pubs.acs.org/acschemicalbiology

Articles

Sulfation Code and Conformational Plasticity of L-Iduronic Acid Homo-Oligosaccharides Mimic the Biological Functions of Heparan Sulfate

Chethan D. Shanthamurthy, Ana Gimeno, Shani Leviatan Ben-Arye, Nanjundaswamy Vijendra Kumar, Prashant Jain, Vered Padler-Karavani,* Jesús Jiménez-Barbero,* and Ragahvendra Kikkeri*

Cite This: *ACS Chem. Biol.* 2021, 16, 2481−2489

Read Online

ACCESS | Metrics & More | Article Recommendations | Supporting Information

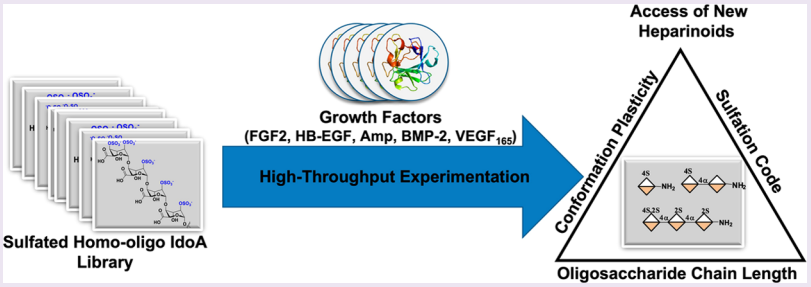

ABSTRACT: Recently, the activity of heparan sulfate (HS) has led to the discovery of many drug candidates that have the potential to impact both medical science and human health. However, structural diversity and synthetic challenges impede the progress of HS research. Here, we report a library of novel L-iduronic acid (IdoA)-based HS mimics that are highly tunable in conformation plasticity and sulfation patterns to produce many of the functions of native HS oligosaccharides. The NMR analysis of HS mimics confirmed that 4-*O*-sulfation enhances the population of the $^1C_4$ geometry. Interestingly, the $^1C_4$ conformer becomes exclusive upon additional 2-*O*-sulfation. HS mimic microarray binding studies with different growth factors showed that selectivity and avidity are greatly modulated by the oligosaccharide length, sulfation code, and IdoA conformation. Particularly, we have identified 4-*O*-sulfated IdoA disaccharide (**I-21**) as a potential ligand for vascular endothelial growth factor ($VEGF_{165}$), which in a multivalent display modulated endothelial cell proliferation, migration, and angiogenesis. Overall, these results encourage the consideration of HS mimics for therapeutic applications.

INTRODUCTION

The nearly 100 years of progress in heparan sulfate/heparin (HS/HP) research has led to numerous advances in the development of anticoagulants and in cancer theranostics.[1−3] Nonetheless, complete utilization of HS/HP in clinical settings remains elusive due to the structural heterogeneity and the inability to synthesize all possible HS oligosaccharides.[4−6] For example, despite the emergence of efficient chemical and enzymatic methods to synthesize HS oligosaccharides, only a small number of synthetic HS analogs have been reported.[7−9] These challenges are further exacerbated by the limited ability to structurally characterize them and track their biological functions.[10] The recognition of HS by the myriad of protein surfaces[11,12] is modulated by its four key inherent structural aspects, (a) sulfation patterns (*O*- and *N*-sulfation),[13−15] (b) uronic acid composition (L-iduronic acid (IdoA) and D-glucuronic acid),[16] (c) oligosaccharide chain length,[11,12,17] and (d) conformation plasticity of IdoA.[18−22] These four factors dictate the ability of a specific HS domain to bind proteins, challenging the discovery of specific HS structural domains to modulate individual heparan sulfate binding protein (HSBP) activity. This challenge has spurred the development of biomimetic analogs of HS and their study in molecular recognition processes. Several HS mimics have been reported in the literature.[23−29] However, they do not provide the structural variation needed to produce multiple functions like the native HS does. Thus, HS biomimetic analogs offer several advantages. First, the heterogeneity and chemical complexity of native HS can be minimized by a limited number of biomimetic analogs. Second, unlike native HS, biomimetic analogs can be designed with pure IdoA residues. This exposes IdoA at reducing and nonreducing ends of the oligosaccharides, giving a unique scaffold to study the conformation plasticity of IdoA at different positions. Here, we report the

Received: July 27, 2021
Accepted: September 15, 2021
Published: September 29, 2021

Scheme 1. Synthesis of Mono- and Di-IdoA Analogs: (a) Azidoethoxyethanol, NIS, TfOH, 4 Å M.S., −10 °C; (b) for I-10 and I-20: LiOH, THF/MeOH/H_2O (4:2:1); $Pd(OH)_2$, MeOH; for I-11 and I-21: NH_2-NH_2.H_2O, AcOH, DCM/MeOH; SO_3.Et_3N, DMF 60 °C; LiOH, THF/MeOH/H_2O (4:2:1); $Pd(OH)_2$, MeOH; for I-12 and I-23: LiOH, THF/MeOH/H_2O (4:2:1); SO_3.Et_3N, DMF 60 °C; $Pd(OH)_2$, MeOH; (c) NIS, TMSOTf, CH_2Cl_2, 4 Å M.S., −10 °C; (d) $Cu(OTf)_2$, Ac_2O, 0 °C; (e) TMSSPh, ZnI_2, CH_2Cl_2, RT; (f) *P*-TsOH, CH_2Cl_2/MeOH(1:1); (g) TEMPO, BAIB, CH_2Cl_2/H_2O (1:1); BnBr, TBAI, $NaHCO_3$, DMF, 60 °C

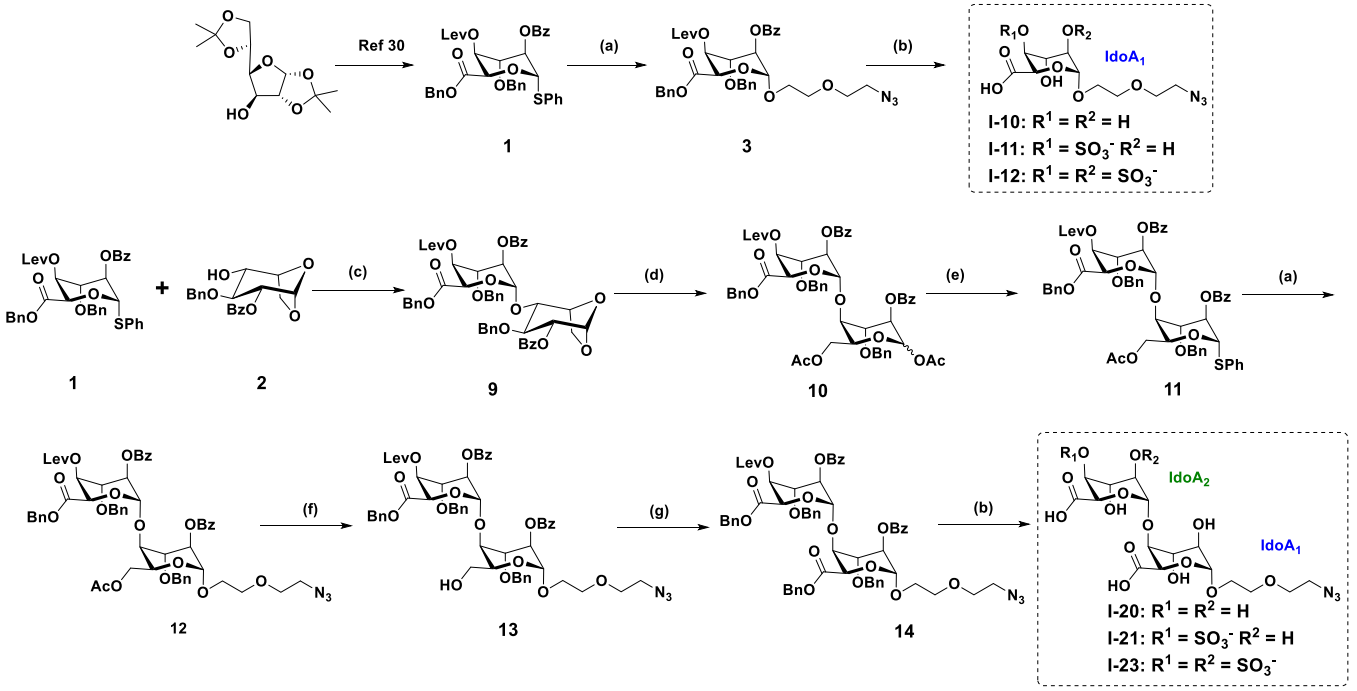

synthesis of a novel, IdoA-based library of HS mimics, which enables the analysis of multiple parameters, including sulfation patterns, conformation plasticity, and oligosaccharide chain length, to establish a structure−function relationship with growth factors and to modulate biological functions. While most current biomimetic designs are composed of natural and unnatural components to decipher structure−function relationships, we synthesized 4-*O*-sulfated analogs in addition to that of nonsulfated and highly sulfated HS mimics. As a prototype, we describe the synthesis of a library of four nonsulfated (**I-10**, **I-20**, **I-30**, and **I-40**), nonreducing end four 4-*O*-sulfated (**I-11**, **I-21**, **I-31**, and **I-41**), and four highly sulfated (**I-12**, **I-23**, **I-34**, and **I-45**) IdoA ligands that mimic the essential structural features of native HS. Extensive nuclear magnetic resonance (NMR) studies, glycan microarrays, and surface plasmon resonance (SPR) binding assays established the relationship between the binding activity of several growth factors, the conformation of IdoA, and sulfation codes. Candidates with high affinities and specificities to vascular endothelial growth factor ($VEGF_{165}$) were cross-linked with star shape dendrimers, and systematic antiangiogenic properties were investigated. The results uncovered a novel avenue for developing HS mimics to target HSBPs and influence drug discovery.

RESULTS AND DISCUSSION

Synthesis of mono-IdoA derivatives (**I-10**, **I-11**, and **I-12**) was carried out using thiophenyl iduronic acid donor **1**. Compound **1** was synthesized with an overall yield of 0.31% from 1,2:5,6-di-*O*-isopropylidene α-D-glucofuranose by a nine-step sequence.[30−32] The stereoselective linker glycosylation of **1** followed by global or selective deprotection and sulfation by using a SO_3.Et_3N complex yielded mono-IdoA derivatives. Di-IdoA derivatives (**I-20**, **I-21**, and **I-23**) were synthesized by stereoselective α-(1,4)-linkage between iduronic acid-thiophenol **1** and 1,6-anhydro-β-L-idopyranosyl 4-alcohol **2** building blocks, respectively. This was followed by subsequent modification of reducing end Idose residues by a previously described protocol with slight modification to improve the overall yield (Scheme 1).[30] Briefly, the anhydro-ring of **9** was subjected to acetolysis in the presence of copper(II) trifluoromethanesulfonate [$Cu(OTf)_2$] and acetic anhydride[33] followed by regioselective glycosylation by using trimethyl(phenylthio)silane in the presence of ZnI_2. Then, we performed linker glycosylation before one-pot oxidation and benzyl esterification in the presence of TEMPO and benzyl bromide to yield fully protected di-IdoA precursor **14**. This synthetic route improved the overall yield and also avoided poisoning the thiophenol donor by TEMPO oxidation.[30] Finally, global or selective deprotection, sulfation, and hydrogenolysis yielded desired di-IdoA analogs. Tri-IdoA derivatives (**I-30**, **I-31**, and **I-34**) were synthesized by glycosylating donor **11** and acceptor **2** (Scheme 2) followed by selective deacetylation of **20** under mild acidic conditions followed by oxidation and esterification.

Finally, the IdoA residue at the reducing end of **22** was subjected to a series of five linear reactions as mentioned above to yield tri-IdoA precursor **27**, which was selectively or globally deprotected and sulfated to obtain desired tri-IdoA derivatives. A similar successive reaction with tri-IdoA donor **24** and acceptor **2** yielded desired tetra-IdoA analogs (**I-40**, **I-41**, and **I-45**). All sulfated-IdoA derivatives were purified by ion-exchange resin chromatography and eluted through a C-18

https://doi.org/10.1021/acschembio.1c00582
ACS Chem. Biol. 2021, 16, 2481−2489

Scheme 2. Synthesis of Tri- and Tetra-IdoA Analogs: (a) NIS, TMSOTf, CH_2Cl_2, 4 Å M.S., −10 °C; (b) *P*-TsOH, CH_2Cl_2/MeOH (1:1); (c) TEMPO, BAIB, CH_2Cl_2/H_2O (1:1); BnBr, TBAI, $NaHCO_3$, DMF, 60 °C; (d) $Cu(OTf)_2$, Ac_2O, 0 °C; (e) TMSSPh, ZnI_2, CH_2Cl_2, RT; (f) Azidoethoxyethanol, NIS, TfOH, 4 Å M.S., −10 °C; (g) for I-30 and 1-40: LiOH, THF/MeOH/H_2O; $Pd(OH)_2$, MeOH; for I-31 and I-41: NH_2-NH_2.H_2O, AcOH, DCM/MeOH; SO_3.Et_3N, DMF 60 °C; LiOH, THF/MeOH/H_2O (4:2:1); $Pd(OH)_2$, MeOH; for I-34 and I-45: LiOH, THF/MeOH/H_2O (4:2:1); SO_3.Et_3N, DMF 60 °C; $Pd(OH)_2$, MeOH

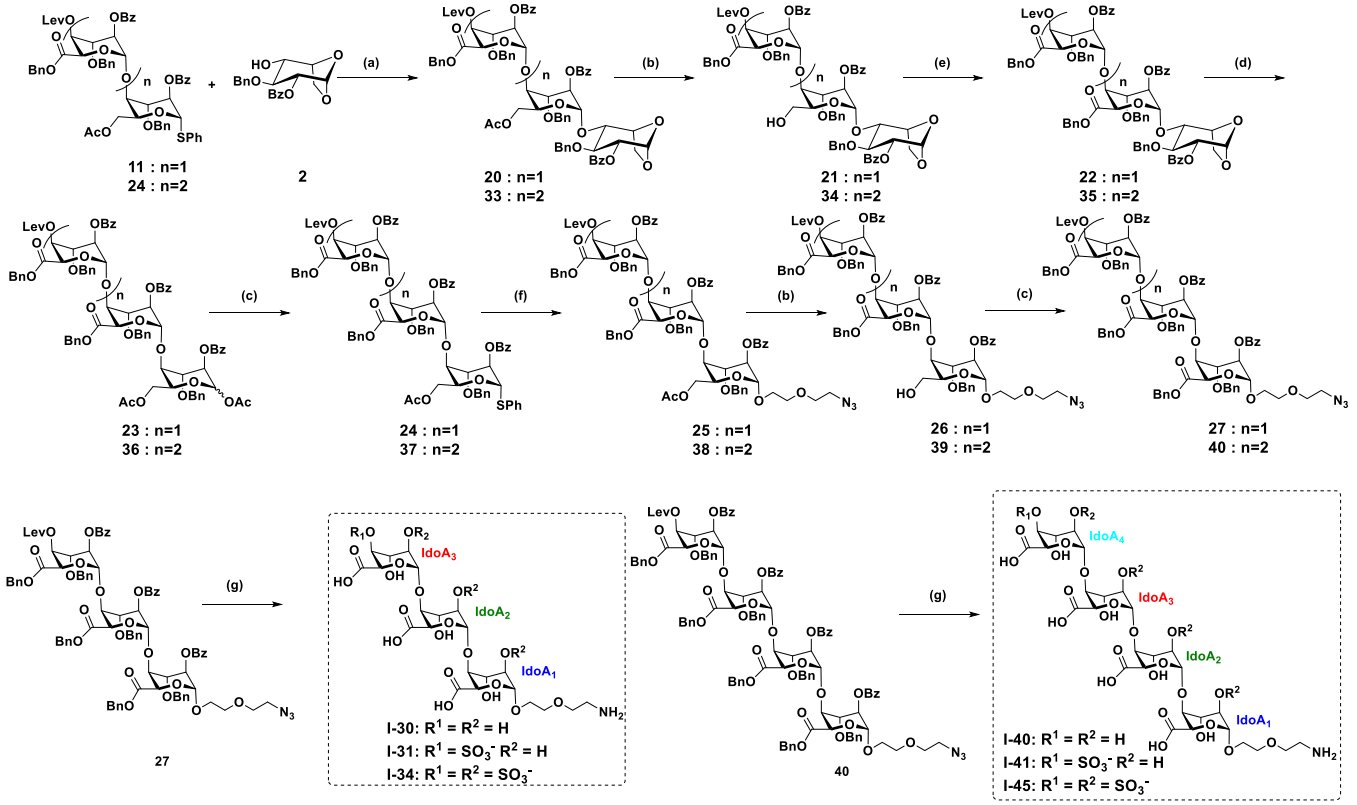

column, and their structures were confirmed by standard NMR and mass spectrometry techniques.

To decipher the conformational plasticity of the IdoA ring in these molecules and the effect of the sulfation pattern on their three-dimensional shapes, the conformational features of the monosaccharide series were first analyzed. The typical approach involves derivation of model $^1C_4$, $^4C_1$, and $^2S_0$ geometries, calculation of key NMR expected parameters [usually Nuclear Overhauser Effect (NOE) and J data], and then fitting them to the experimental values.

The population combination that provides the best fit is assumed to be the actual conformational distribution in solution. However, this approach suffers from some intrinsic caveats, since the intrinsic mobility of the $^2S_0$ conformer makes it very difficult to estimate the exact J and NOE data.[34] Nevertheless, NOE-derived distances between H2 and H5 within the IdoA ring have been traditionally used as an estimation of the relative population of the $^2S_0$-form.[35] In fact, the existence of short distance between H2 and H5 protons, ca. 2.5 Å, and, therefore, the presence of NOE are a unique feature of the $^2S_0$ geometry (Figure 1a). However, slight variations around the basic skew-boat geometry modify all the intraring proton−proton distances, including the H2−H5 ones, and thus strongly hamper the quantitative analysis of the NOEs. Although H1−H3 and H2−H4 NOEs are expected to be much stronger in the $^4C_1$ chair, the corresponding distances are also smaller than 3 Å in the $^2S_0$ alternative. Moreover, the existence of motional anisotropy can also hamper the extraction of accurate proton−proton distances,[46] making the NOE-based quantitative analysis of the conformational distribution of IdoA rings far from trivial. In addition, the derivation of the expected $^3J_{HH}$ couplings for the basic geometries also suffers from diverse drawbacks.

The application of the "best" Karplus-type equations to the basic conformers also provides errors due to the intrinsic approximations of the equations, due to the possible distortions that take place upon sulfation, and due to the existing fluctuations of the molecules, especially around the skew boat form.[34] Herein, we have compared the data extracted from the independent analysis of NOEs and Js to provide an integrated answer. Once the conclusions were reached for the monosaccharide series, the protocol was performed for the oligosaccharides. In particular, the key proton−proton distance information that encodes the distribution of the different conformers was extracted from the two-dimensional Nuclear Overhauser SpectroscopY (2D-NOESY) experiments. Key NOEs, including H2−H5 (exclusive for $^2S_0$), H1−H2 (shorter distance in $^1C_4$), H1−H3 and H2−H4 (shorter distances in $^4C_1$), and H4−H5 (always fairly short, between 2.3 and 2.4 Å), were considered and employed to estimate a relative population of conformers for each molecule by least square analysis (see Table S26 and Table 1). A somehow different estimation of the population of conformers was also derived from the analysis of the vicinal $^3J_{HH}$ coupling constants. Finally, the conclusions of the NOE analysis were compared to those from the J-based approach to

https://doi.org/10.1021/acschembio.1c00582
ACS Chem. Biol. 2021, 16, 2481−2489

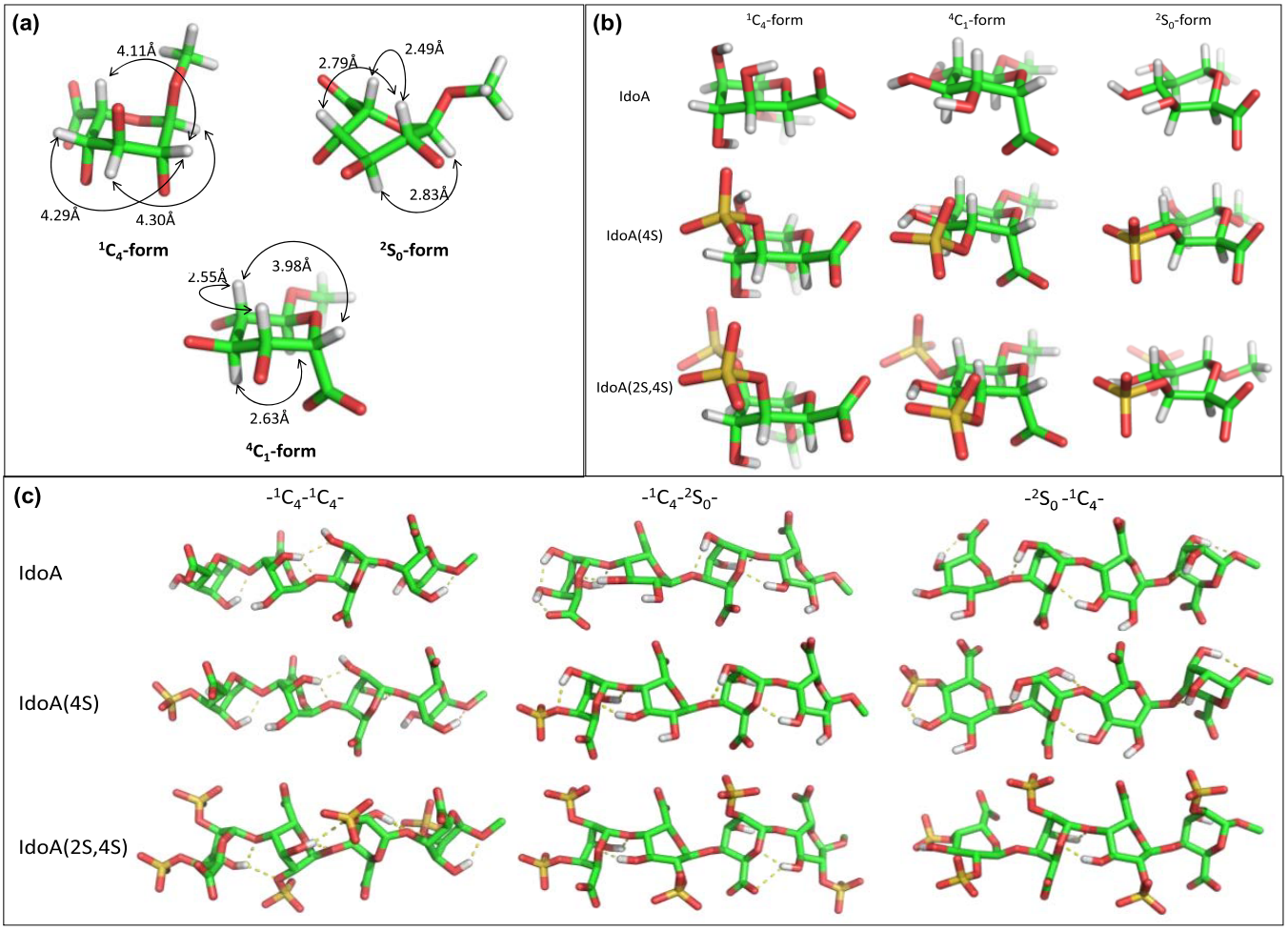

Figure 1. Molecular modeling of IdoA: (a) structures of $^1C_4$, $^4C_1$, and $^2S_0$ conformers of IdoA. Distinguishing proton−proton distances for each conformer are indicated by arrows; (b) DFT-optimized geometries of $^1C_4$, $^4C_1$, and $^2S_0$ conformers for nonsulfated, 4-sulfated, and 2,4-sulfated IdoA monosaccharides; (c) modeled geometries for **I-40**, **I-41**, and **I-45**. $^1C_4$−$^1C_4$, $^1C4$−$^2S_0$, and $^2S_0$−$^1C_4$ pairs were considered on the basis of NOE data. Intraresidue and inter-residue hydrogen contacts were indicated.

propose the conformational equilibria for the 12 analogs (Table 1). The complete analysis is gathered in the Supporting Information. The analysis of the NOE and J data for monosaccharides **I-10**, **I-11**, and **I-12** showed a clear correlation between the sulfation pattern and the population of the $^1C_4$ conformer. According to both the J and NOE-based analysis, for the nonsulfated IdoA, **I-10**, the $^4C_1$ conformer was predominant (ca. 60−65%). Interestingly, in **I-11**, sulfation at *O*-4 produced a population shift (50%) toward the $^1C_4$ form, decreasing the $^4C_1$ chair (20−30%). The population of the $^2S_0$ skew boat remained between 15 and 30%.

Strikingly, the analysis of the NMR data for **I-12** showed that the introduction of the 2-*O*-sulfate group brought about a dramatic decrease in the populations of the $^2S_0$ and $^4C_1$ forms (less than 10%) favoring the $^1C_4$ conformer, which is now populated in more than 90%. Both NOE data and coupling constants are in agreement with this population distribution (see Tables S5−S7). For **I-10**, it can be speculated that stabilizing hydrogen-bonding and/or ionic interactions between OH3 and OH4 favor the $^2S_0$ and $^4C_1$ conformers.[22] In contrast, the 4-*O*-sulfate group prefers to be accommodated in the $^1C_4$ form, although according to the population distribution, the free energy difference with the other $^4C_1$ and $^2S_0$ conformers remains minimal (Figure 1b). The new interaction between OH2 and 4-*O*-SO_3 in the $^1C_4$ geometry may account for this slight shift. However, the presence of the double sulfation at *O*-2 and *O*-4 completely shifts the equilibrium toward the $^1C_4$ conformer. The dipole moment of this geometry for **I-12** is the largest of all possible geometries and would be highly favored in aqueous environments. Taken together, these results point out that at the monosaccharide level, 4-*O*-sulfation slightly favors the $^1C_4$-IdoA geometry, whereas double sulfation at *O*-2 and *O*-4 drives the $^1C_4$ chair conformation to be the most favorable one (Figure 1b). A similar approach was employed to analyze the ring pucker in the di-, tri-, and tetra IdoA-ligands (Table 1). For the nonsubstituted disaccharides, **I-20**, or for **I-21**, the existence of major conformational plasticity was deduced, with the presence of the three geometries. The $^1C_4$ is slightly predominant and becomes even more populated at IdoA2 of **I-21** upon sulfation at *O*-4 (>70%). Nevertheless, there are always notorious participations of the $^2S_0$ and $^4C_1$ forms. In fact, both NMR approaches, NOE- and J-based, showed that the conformational plasticity present in **I-10** and **I-11** monosaccharides is retained in the disaccharide series. Sulfation at *O*-2 (**I-23**) increases the populations of the $^1C_4$ chair at both rings (ca. 90%). A similar trend was observed for the trisaccharide and tetrasaccharides. It may be inferred that

https://doi.org/10.1021/acschembio.1c00582
ACS Chem. Biol. 2021, 16, 2481−2489

Table 1. Conformation Plasticity of IdoA in Monosaccharides I-10, I-11, and I-12 and Different IdoA Rings in the Studied Oligosaccharides[a]

	monosaccharides				disaccharides					
	population[b]				population IdoA2			population IdoA1		
	$^1C_4$	$^4C_1$	$^2S_0$		$^1C_4$	$^4C_1$	$^2S_0$	$^1C_4$	$^4C_1$	$^2S_0$
I-10	19 ± 4/8 ± 5 **13 ± 8**	67 ± 7/60 ± 4 **63 ± 5**	15 ± 10/33 ± 5 **24 ± 13**	**I-20**	56 ± 11	24 ± 22	20 ± 11	59 ± 10	8 ± 8	33 ± 18
I-11	50 ± 4/50 ± 4 **50 ± 4**	29 ± 7/18 ± 5 **23 ± 8**	21 ± 10/33 ± 5 **27 ± 8**	**I-21**	71 ± 8	12 ± 14	17 ± 15	50 ± 5	11 ± 15	39 ± 20
I-12	90 ± 5/90 ± 5 **90 ± 5**	5 ± 5/5 ± 5 **5 ± 5**	5 ± 5/5 ± 5 **5 ± 5**	**I-23**	89 ± 1	4 ± 1	7 ± 2	88 ± 1	3 ± 1	9 ± 2

	trisaccharides								
	population IdoA3			population IdoA2			population IdoA1		
	$^1C_4$	$^4C_1$	$^2S_0$	$^1C_4$	$^4C_1$	$^2S_0$	$^1C_4$	$^4C_1$	$^2S_0$
I-30	54 ± 4	25 ± 12	21 ± 8	75 ± 2	10 ± 9	15 ± 6	54 ± 4	10 ± 8	36 ± 12
I-31	75 ± 1	7 ± 7	19 ± 6	66 ± 8	10 ± 3	24 ± 5	60 ± 4	12 ± 5	28 ± 8
I-34	90 ± 5	5 ± 5	5 ± 5	90 ± 5	5 ± 5	5 ± 5	85 ± 1	5 ± 4	10 ± 3

	tetrasaccharides								
	population IdoA4			population IdoA3/2			population IdoA1		
	$^1C_4$	$^4C_1$	$^2S_0$	$^1C_4$	$^4C_1$	$^2S_0$	$^1C_4$	$^4C_1$	$^2S_0$
I-40	60 ± 2	13 ± 13	27 ± 10	55 ± 7	19 ± 9	26 ± 17	55 ± 9	23 ± 8	22 ± 17
I-41	73 ± 9	16 ± 1	11 ± 11	75 ± 9	9 ± 8	16 ± 17	62 ± 3	20 ± 18	18 ± 21
I-45	85 ± 7	4 ± 1	11 ± 8	87 ± 4	8 ± 4	5 ± 0	81 ± 13	12 ± 10	7 ± 3

[a]The population of each conformer was indicated as an average of the data obtained from NOE and $^3J_{HH}$ analysis. [b]Derived conformer population from J analysis/NOE analysis and average (in bold) was indicated for each compound (Supporting Information tables).

the double *O*-2 and *O*-4 substitution for the internal IdoA2 ring in **I-30** provides a larger population (above 70% for both J- and NOE-based analysis) of the $^1C_4$ chair. Sulfation at *O*-4 of the terminal ring again increases the population of the $^1C_4$ (>70%) at the corresponding residues. In contrast, the $^1C_4$ contribution is highly increased at all rings of **I-34** and **I-45** when sulfation at *O*-2 takes place.

Moreover, the glycosidic linkages provide additional torsional degrees of freedom in these molecules. For heparin and HS oligosaccharides, it has been described that the IdoA-containing glycosidic linkages mainly populate one conformational family on the Φ/Ψ map in the exo-anomeric/syn region.[36,37] Therefore, disaccharide models of the nine possible combinations of the $^2S_0$, $^4C_1$, and $^1C_4$ geometries were built for **I-20**, as the basic scaffold of all the oligosaccharides (see Figure S18), submitted to energy minimization, and the global minima for each combination were carefully analyzed. Fittingly, in addition to the intraring H2−H5 distance, the H5i + 1-H3i inter-residue contact (where i and i + 1 refer to two contiguous IdoA residues, i being the closer residue to the reducing end of the oligosaccharide chain) also contains conformational information on the shapes of the pyranose rings at the glycosidic linkage. In particular, very close contacts (2.3−2.4 Å) between these two protons are expected only for certain combinations ($^1C_4$−$^1C_4$ and $^1C_4$−$^2S_0$) of the pyranose rings and moderate contacts (2.9−3.0 Å) for the $^2S_0$−$^2S_0$ and $^2S_0$−$^1C_4$ shapes' pairs around the glycosidic linkages. The estimated distances for the other five combinations are longer than 4.5 and mostly beyond 5 Å. Regarding other inter-residue NOEs, the H1i + 1-H4i distance does not significantly depend on the shape of the flanking residues (2.2−2.5 Å), except for the $^4C_1$−$^2S_0$ combination (3.1 Å). However, in this particular case, the H1i + 1-H3i distance would be fairly short (2.3 Å), as in the $^4C_1$−$^1C_4$ arrangement.

Indeed, very strong NOEs were observed for the H1i + 1-H4i proton pairs, corresponding to very short distances (2.0−2.4 Å), which strongly suggested the existence of the typical exo-anomeric/syn conformation around the glycosidic linkages together with a negligible contribution of the $^4C_1$−$^2S_0$ combination. Although very rarely (**I-20**; **I-30**), very weak H1i + 1-H3i NOEs were detected, which also allowed discarding a significant contribution of the $^4C_1$−$^1C_4$ arrangement. In contrast, for most of the glycosidic linkages in most of the analogs, as exemplified in **I-45**, significant H5i + 1-H3i inter-residue NOEs were measured, corresponding to short distances (2.0−2.7 Å) between the corresponding protons pairs (see Table S25). Therefore, this feature supported the presence of major contributions of $^1C_4$−$^1C_4$, $^1C_4$−$^2S_0$, or $^2S_0$−$^1C_4$ pyranose chairs at both sides of the glycosidic linkages, as also deduced from the analysis at the monosaccharide level. Then, NOE-derived NMR distances were employed as restraints to build representative 3D structures of IdoA homo-oligomers and thus to account for the observed conformational preferences and the distinctive role of the 4-*O* and 2-*O*-SO_3 groups. In particular, tetrasaccharides differing in the sulfation pattern and displaying $^1C_4$−$^1C_4$, $^1C_4$−$^2S_0$, and $^2S_0$−$^1C_4$ pairs are depicted in Figure 1c. All nonsulfated, mono-sulfated, and penta-sulfated tetrasaccharides **I-40**, **I-41**, and **I-45** structures displayed inter-residue hydrogen bonds, either between 3-O(i) and 3-OH(i + 1), which may stabilize the $^1C_4$ conformers, or between 3-OH(i) and O5(i + 1), in the case of molecules containing $^2S_0$-skew boat conformers (Figure 1c). These observations made it difficult to disentangle the origin of small energy differences between the possible pyranose forms, and other factors such as those related to polarity effects would contribute to tilt the conformer equilibrium. This effect was completely noticeable when the $^1C_4$ form became predominant after overall sulfation.

https://doi.org/10.1021/acschembio.1c00582
ACS Chem. Biol. 2021, 16, 2481−2489

This conformer allows maintaining the inter-residue hydrogen bonds without generating strong electronic repulsion. In contrast, the $^1C_4$–$^2S_0$ and $^2S_0$–$^1C_4$ pairs would locate the 2-*O*-SO_3 and COOH groups of two adjacent units very close, thus increasing the energy of the corresponding geometry.

With the ability to access either pure $^1C_4$-shape or mixed geometries of mono- and oligo-IdoA ligands, we embarked on a systematic investigation of the role of sulfation patterns and the conformation of IdoA on their recognition by different growth factors (Figure S22), alongside with positive control (natural heparin) and negative control glycans (sialic acid-containing glycans; Sia-glycans). For that, glycan microarrays were used to identify the epitope selectively recognized by the proteins of interest. First, the binding preference of human basic fibroblast growth factor (FGF2) was examined against 12 different HS analogs by nanoprinted glycan microarrays. To facilitate comparison of these high-throughput binding profiles, ranking of binding was computed for each FGF2 dilution. As shown in Figure 2, nonsulfated glycans (**I-10** to **I-40** ranked

Sulfation	Oligomerization	ID	FGF2	HB-EGF	Amph.	BMP2	VEGF
Non	Mono-saccharide	I-10	35	22	52	41	23
	Di-saccharide	I-20	35	25	47	35	13
	Tri-saccharide	I-30	26	22	65	45	8
	Tetra-saccharide	I-40	27	28	59	47	24
Mono-4-*O*-sulfate	Mono-saccharide	I-11	40	55	60	83	89
	Di-saccharide	I-21	54	47	66	91	99
	Tri-saccharide	I-31	57	45	72	73	59
	Tetra-saccharide	I-41	49	20	67	47	5
2,4-*O*-sulfate	Mono-saccharide	I-12	50	79	66	71	72
	Di-saccharide	I-23	63	63	57	74	76
	Tri-saccharide	I-34	97	97	93	73	76
	Tetra-saccharide	I-45	41	48	51	66	70
Natural Heparin			39	58	57	24	84

%
100
75
50
25
0

Figure 2. Growth factor glycan microarray binding assay: Binding was tested at three serial dilutions and then detected with the relevant biotinylated secondary antibody (1 μg/mL) followed by Cy3-strepavidin (1.5 μg/mL) (Supporting Information Appendix Table S27). Arrays were scanned, relative fluorescent units (RFU) were obtained, and then rank binding of growth factors (each at three dilutions) to glycans printed at four replicates each was calculated: for each binding assay per printed block, the maximum RFU was determined and set as 100% binding. Then, binding to all the other glycans in the same block was ranked in comparison to the maximal binding, and the average rank binding (and SEM) for each glycan across the three examined concentrations of each growth factor was calculated. This analysis allowed to compare the glycan binding profiles of the different growth factors and dissect their binding preferences. The mean rank is shown as a heatmap of all the examined binding assays together (red highest, blue lowest, and white 50th percentile of ranking).

35, 35, 26, and 27%, respectively) exhibited weak binding, whereas the mono-4-*O*-sulfated glycans (**I-11** to **I-41** ranked 40, 54, 57, and 49%, respectively) displayed moderate binding. On the other hand, highly sulfated IdoA ligands (**I-12** to **I-34** ranked 50, 63, and 97%, respectively) showed moderate to stronger binding with increasing oligosaccharide length. Interestingly, **I-45** displayed reduced binding (ranked 41%).

Similar results were observed for the heparin binding epidermal growth factor (HB-EGF) and amphiregulin (Figure 2), which are both classified as ligands that bind EGF receptors (EGFRs).[38,39] Of note, FGF2 showed low binding to all four negative control Sia-glycans. In contrast, bone morphogenic protein-2 (BMP2) and $VEGF_{165}$, a key synergistic mediator in osteogenesis and angiogenesis,[40,41] exhibited unexpected strong binding to **I-11** and **I-21** (ranked 83 and 91% with BMP2 and 88 and 99% with $VEGF_{165}$), whereas **1**–**31** and **I-41** displayed moderate to poor binding (ranked 73 and 47% with BMP2 and 59 and 5% with $VEGF_{165}$). Of note, the binding to intermediate sulfated analogs was higher than the binding to natural heparin, and binding to Sia-glycan negative control was low. Based on these findings, **I-11** and **I-21** were identified as simple and highly efficient unnatural carbohydrate ligands to target BMP2 and $VEGF_{165}$. Additional SPR binding experiments to further support the microarray data were performed by immobilizing **I-21** on CM5 gold chips and determining real-time binding affinities with $VEGF_{165}$ and BMP-2. The K_D values of **I-21** with $VEGF_{165}$ and BMP-2 were 10.27 and 3.15 μM, respectively (Figure 3a,b).

Regarding a putative structure–function relationship, the binding analysis with a series of growth factors (FGF2, HB-EGF, and amphiregulin) showed that the optimum length of the tested ligands is in the trisaccharide range with a high sulfation content. This molecule displays an almost exclusive $^1C_4$ shape for the different rings. Interestingly, HS-GAG tetrasaccharide displaying a trisaccharide kink with a $^1C_4$ IdoA has been suggested to be the minimal binding motif for FGF2.[42] A 3D model of the possible complex between FGF2 and **I-34** is shown in the Supporting information (Figure S20). Alternatively, other growth factors ($VEGF_{165}$ and BMP-2) prefer the small monosaccharide and disaccharide entities, with intermediate sulfate content. In these cases, both molecules display a wide conformational equilibrium in the IdoA rings with participation of the three conformers (Figure S21). These data confirm the importance of conformational plasticity to modulate the interactions of HS and its analogs with their receptors.

The biological significance of HS mimics was further evaluated by constructing the HS mimic glycodendrimer **D-I21**, as the multivalent display of HS ligands significantly enhances HSBP activity.[43−47] The glycodendrimers were synthesized by the reaction of the **I-21** amine linker with the active carboxylic acid ester of the star dendrimer. The desired glycodendrimer was purified by centrifugation with a 3 kDa ultrafiltration device. The conjugation of the HS mimic was determined by ^1H and ^{13}C-NMR, which display the stoichiometric 1:4 loading of **I-21** on each dendrimer unit. Similarly, the negative control dendrimer, **D-L** (Figure 3c), was also synthesized and characterized. Using these two dendrimers, the degree to which the proliferation of endothelial cells was inhibited in the presence of $VEGF_{165}$ was measured. **D-I21** displayed a stronger inhibition of cell proliferation in a dose-dependent manner compared to **D-L** (Figure 3d). To determine the mechanism that inhibits cell proliferation, western blot analysis of phosphorylated (Tyr951) vascular endothelial growth factor receptor-2 (VEGFR-2) in the presence of different concentrations of **D-I21** (25 and 50 μg/mL) and $VEGF_{165}$ (20 ng/mL) was performed (Figure 3e and Figure S23). It was hypothesized that the strong binding between $VEGF_{165}$ and **D-I21** will inhibit $VEGF_{165}$-dependent VEGFR-2 phosphorylation.[48] A concentration of 50 μg/mL of **D-I21** caused a significant reduction in the phosphorylation of VEGFR-2, indicating that **D-I21** is directly involved in the VEGF-mediated biological activity. To further verify VEGF/**I-21** cellular activity, cell migration analysis was performed. As expected, the addition of **D-I21** (50 μg/mL) to $VEGF_{165}$-

https://doi.org/10.1021/acschembio.1c00582
ACS Chem. Biol. 2021, 16, 2481−2489

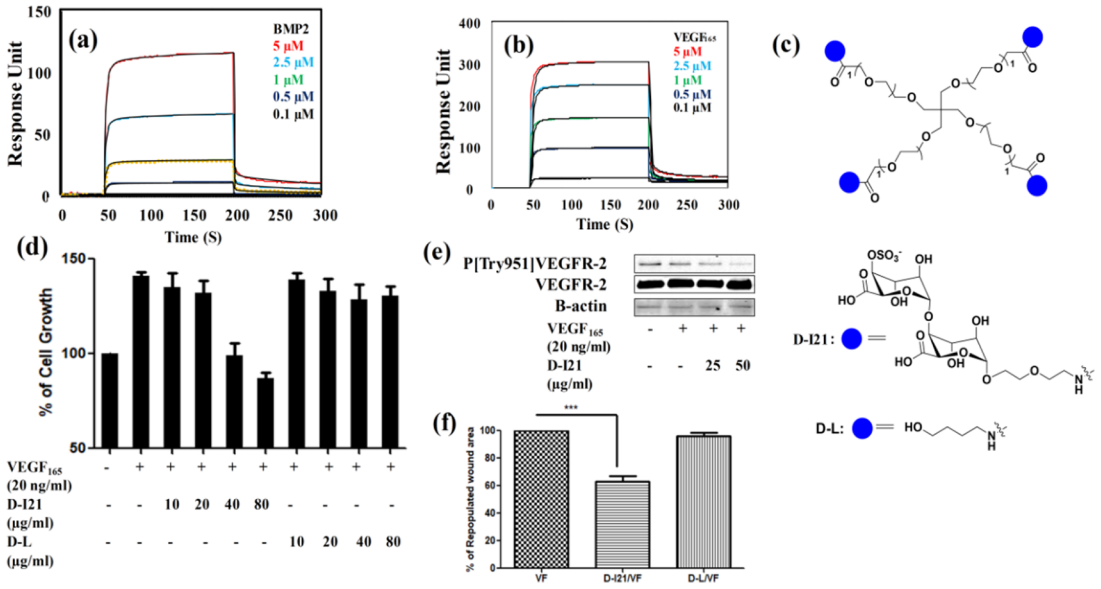

Figure 3. Endothelial tube inhibition assay: (a) SPR binding analysis of the interaction between BMP-2 and **I-21** (concentration of BMP-2 was 0.1−5 μM; dissociation constant (K_D) is 10.27 ± 0.3 μM, k_{on} of 3.37 ± 0.2 × 104 M^{-1} s^{-1}, and k_{off} of 3.46 ± 0.12 × 10^{-1} s^{-1}; (b) dissociation constant (K_D) of $VEGF_{165}$ and **I-21** is 3.15 ± 0.7 μM, k_{on} of 5.78 ± 0.2 × 104 M^{-1} s^{-1}, and k_{off} of 1.83 ± 0.5 × 10^{-1} s^{-1}; (c) structure of star-shaped dendrimers **D-I21** and **D-L**; (d) effect of the HS mimic glycodendrimer on human umbilical vein endothelial cell (HUVEC) proliferation in the presence of $VEGF_{165}$ growth factors. Cell proliferation was evaluated using the SRB assay. Cell growth without growth factors is considered as control (100%). Results are represented as the mean SD (n = 3); (e) effect of **D-I21** on VEGFR-2 phosphorylation; (f) effect of **D-I21** and **D-L** on the HUVEC migration assay in the presence of $VEGF_{165}$. The concentration of dendrimers is 50 μg/mL, and the concentration of $VEGF_{165}$ is 20 ng/mL (n = 3).

treated HUVECs significantly reduced cell migration in the wound healing assay (Figure 3f).[49] Collectively, these results establish that **I-21** dendrimers may provide opportunities in regenerative medicine and tissue repair and in discovering a novel therapeutic agent for cancer.

CONCLUSIONS

In conclusion, the synthesis of a new set of HS mimics by utilizing IdoA scaffolds and sulfation patterns is described herein. Extensive NMR studies confirmed that the sulfation code modulates the shape of the IdoA ring and provides a rational approach to enhance the population of the $^1C_4$ conformations. Microarray and SPR-based binding assays with various growth factors have revealed that the sulfation code and the optimal homo-oligosaccharide length synergistically modulate the binding specificity. Previous $VEGF_{165}$-HS interactions have shown that HS hexasaccharides with unique sulfation patterns are the minimum necessary sequence for binding to $VEGF_{165}$.[50] However, our results reveal that simple disaccharide entities (**I-21**) with unusual conformation plasticity and sulfation patterns can selectively interact with $VEGF_{165}$ and thereby modulate angiogenesis activity. These results open a new avenue for generating structurally well-defined HS mimics using IdoA scaffolds with similar functions of native heparin/HS.

METHODS

General Remarks. All NMR experiments were performed at 10−35 °C using a Bruker AVANCE 2600 MHz spectrometer equipped with a standard triple-channel probe. Samples (500uL) with typical concentrations of 1−5 mM were prepared by dissolving the purified compounds in D_2O. ^{1}H-NMR resonances of monosaccharides **I-10**, **I-11**, and **I-12**, disaccharides **I-20**, **I-21**, and **I-23**, trisaccharides **I-30**, **I-31**, and **I-34**, and tetrasaccharides **I-40**, **I-41**, and **I-45** were assigned through standard TOCSY (60 and 90 ms mixing times), NOESY (50−500 ms mixing times), ROESY, and HSQC experiments. ^{1}H-NMR assignment results are provided in Figures S1−S4 and Tables S1−S4.

Conformational Analysis. 2D-NOESY experiments of mono-, di-, tri-, and tetramers of IdoA were performed at 600 MHz (mixing time varying between 250 and 600 ms). NOE-derived distances for proton−proton pairs were calculated following the isolated spin pair approximation and compared with the theoretical distance of the pure conformers. Intraresidue NOE cross-peaks between H4 and H5 were used as the reference. $^1C_4$, $^4C_1$, and $^2S_0$ conformer distribution was estimated by least sum of square difference analysis of the calculated and experimental NOE intensity and $^3J_{HH}$. The theoretical distances and thus NOE intensities were calculated for DFT-optimized geometries of nonsulfated, mono-sulfated, and di-sulfated IdoA monosaccharides, whereas reported theoretical $^3J_{HH}$ values for IdoA(2S)[22] were employed for the analysis based on coupling constants. The residual sum of squares (RSS) was used to determine how well the calculated population ratios fit the experimental data. Moreover, the estimated population was indicated as an average of the 10 conformer distributions with the lowest RSS. The standard deviation was used to estimate the error in the determined values. Finally, conformer distribution was indicated as an average of the populations derived from analysis of NOE and $^3J_{HH}$ data.

SPR Binding Kinetics. **I-21** and the propanol amine linker (control cell) (1 mM) were covalently immobilized on the CM5 sensor surface using a coupling and active ester and amine coupling reaction. For K_D experiments, immobilized **I-21** (0.5 mM) and the control linker (negative control 0.5 mM) was treated with different growth factors at a flow rate of 50 μL/min and 25 °C. HBS-EP buffer without growth factors was then flowed over the sensor surface for 3 min to enable dissociation. Kinetic analysis was performed using the BIAevaluation software for T100. Association and dissociation phase data were globally fitted to a simple 1:1 interaction model.

Cell Proliferation Assay. HUVECs were plated on 24-well plates in an EBM-2 medium in 1% FBS without growth supplements. The cells were incubated for 4 h before the experiments. Dendrimers (**D-I21** and **D-L**) at different concentrations (10−80 μg/mL) were

https://doi.org/10.1021/acschembio.1c00582
ACS Chem. Biol. 2021, 16, 2481−2489

preincubated with $VEGF_{165}$ (20 ng/mL) and added to the cells. After 48 h of incubation, the cells were washed and fixed with paraformaldehyde. The cells were stained with 4% sulforhodamine B in 1% acetic acid for 30 min and washed with 1% acetic acid solution. The cells were dissolved in 200 mL of 10 mM Tris pH 8.8 and transferred to a 96-well plate for reading on a microplate reader at 540 nm.

Wound Healing Assay. HUVECs were cultured on 24-well plates with EBM-2 media. After monolayer formation, a wound was created by using a 1000 μL pipette tip. The cells were then treated with **D-I21** (50 μg/mL) and $VEGF_{165}$ or $VEGF_{165}$ alone (20 ng/mL). After 12 h, $VEGF_{165}$-treated monolayers showed complete wound healing, which was considered as 100% wound healing, and at that point, the percentage of the cells migrated in other wells was quantified.

Western Blotting. HUVECs were cultured in EBM-2 having 20 ng/mL of $VEGF_{165}$ and different concentrations of **D-I21** (25 and 50 μg/mL) for 1 h at 37 °C. The cells were then lysed. The cell extracts were subjected to sodium dodecyl sulfate−polyacrylamide gel electrophoresis and later transferred to polyvinylidene difluoride membranes. The membranes were incubated with a primary antibody (against β-actin, VEGF receptor-2, or pVEGF receptor-2 [Tyr 951]) for 24 h at 4 °C. Then, they were incubated for 1 h at room temperature with horseradish peroxidase-conjugated respective secondary antibody and finally developed by using a chemiluminescent substrate.

■ ASSOCIATED CONTENT

Supporting Information

The Supporting Information is available free of charge at https://pubs.acs.org/doi/10.1021/acschembio.1c00582.

Experimental procedures and materials, including detail NMR studies; microarray analysis; computational studies; and ^{1}H NMR and ^{13}C NMR spectra for reported compounds (PDF)

■ AUTHOR INFORMATION

Corresponding Authors

Vered Padler-Karavani − *Department of Cell Research and Immunology, The Shmunis School of Biomedicine and Cancer Research, The George S. Wise Faculty of Life Sciences, Tel Aviv University, Tel Aviv 69978, Israel;* orcid.org/0000-0002-4761-3571; Email: vkaravani@tauex.tau.ac.il

Jesús Jiménez-Barbero − *CIC bioGUNE, Basque Research Technology Alliance, BRTA, 48160 Derio, Spain; Ikerbasque, Basque Foundation for Science, 48009 Bilbao, Spain; Department Organic Chemistry II, Faculty of Science and Technology, UPV-EHU, 48940 Leioa, Spain;* orcid.org/0000-0001-5421-8513; Email: jjbarbero@cicbiogune.es

Ragahvendra Kikkeri − *Indian Institute of Science Education and Research, Pune 411008, India;* orcid.org/0000-0002-4451-6338; Email: rkikkeri@iiserpune.ac.in

Authors

Chethan D. Shanthamurthy − *Indian Institute of Science Education and Research, Pune 411008, India*

Ana Gimeno − *CIC bioGUNE, Basque Research Technology Alliance, BRTA, 48160 Derio, Spain;* orcid.org/0000-0001-9668-2605

Shani Leviatan Ben-Arye − *Department of Cell Research and Immunology, The Shmunis School of Biomedicine and Cancer Research, The George S. Wise Faculty of Life Sciences, Tel Aviv University, Tel Aviv 69978, Israel*

Nanjundaswamy Vijendra Kumar − *Indian Institute of Science Education and Research, Pune 411008, India; Department of Chemistry, JSS College of Arts, Commerce & Science, Mysuru 570025, India*

Prashant Jain − *Indian Institute of Science Education and Research, Pune 411008, India*

Complete contact information is available at: https://pubs.acs.org/10.1021/acschembio.1c00582

Notes

The authors declare no competing financial interest.

■ ACKNOWLEDGMENTS

Financial support from the IISER, Pune, DST (Grant No. SR/NM/NS-1113/2016), DBT (Grant No. BT/PR21934/NNT/28/1242/2017), STARS/APR2019/CS/426/FS, and SERB/F/9228/2019-2020 are gratefully acknowledged (to R.K.). The group at CIC bioGUNE thanks the European Research Council (RECGLYCANMR, Advanced Grant no. 788143), ISCIII (Grant PRB3 IPT17/0019 to AG), and the Agencia Estatal de Investigación (Spain) for Grant RTI2018-094751-B-C21 and the Severo Ochoa Excellence Accreditation (SEV-2016-0644). This work was also supported by the Israeli Science Foundation (ISF; to V.P-K.). We thank J. Gallanger for valuable suggestions and future collaboration.

■ REFERENCES

(1) Wardrop, D.; Keeling, D. The story of the discovery of heparin and warfarin. *Br. J. Haematol.* **2008**, *141*, 757−763.

(2) Bishop, J. R.; Schuksz, M.; Esko, J. D. Heparan sulphate proteoglycans fine-tune mammalian physiology. *Nature* **2007**, *446*, 1030−1037.

(3) Varki, A.; Cummings, R. D.; Esko, J. D.; Stanley, P.; Hart, G. W.; Aebi, M.; Darvill, A. G.; Kinoshita, T.; Packer, N. H.; Prestegard, J. H.; Schnaar, R. L.; Seeberger, P. H. *Essentials of Glycobiology*; 3rd ed.; Cold Spring Harbor Laboratory Press: Cold Spring Harbor, NY, 2015.

(4) Lever, R.; Page, C. P. Novel drug development opportunities for heparin. *Nat. Rev. Drug. Discov.* **2002**, *1*, 140−148.

(5) Esko, J. D.; Lindahl, U. Molecular diversity of heparan sulfate. *J. Clin. Investig.* **2001**, *108*, 169−173.

(6) Shriver, Z.; Capila, I.; Venkataraman, G.; Sasisekharan, R. Heparin and heparan sulfate: analyzing structure and microheterogeneity. *Handb. Exp. Pharmacol.* **2012**, *207*, 159−176.

(7) Mende, M.; Bednarek, C.; Wawryszyn, M.; Sauter, P.; Biskup, M. B.; Schepers, U.; Bräse, S. Chemical Synthesis of Glycosaminoglycans. *Chem. Rev.* **2016**, *116*, 8193−8255.

(8) Tsai, C. T.; Zulueta, M.; Hung, S. C. Synthetic heparin and heparan sulfate: probes in defining biological functions. *Curr. Opin. Chem. Biol.* **2017**, *40*, 152−159.

(9) Xu, D.; Arnold, K.; Liu, J. Using structurally defined oligosaccharides to understand the interactions between proteins and heparan sulfate. *Curr. Opin. Chem. Biol.* **2018**, *50*, 155−161.

(10) Shajahan, A.; Heiss, C.; Ishihara, M.; Azadi, P. Glycomic and glycoproteomic analysis of glycoproteins-a tutorial. *Anal. Bioanal. Chem.* **2017**, *409*, 4483−4505.

(11) Capila, I.; Linhardt, R. J. Heparin-protein interactions. *Angew. Chem., Int. Ed.* **2002**, *41*, 390−412.

(12) Xu, D.; Esko, J. D. Demystifying heparan sulfate-protein interactions. *Annu. Rev. Biochem.* **2014**, *83*, 129−157.

(13) Soares da Costa, D.; Reis, R. L.; Pashkuleva, I. Sulfation of Glycosaminoglycans and Its Implications in Human Health and Disorders. *Annu. Rev. Biomed. Eng.* **2017**, *19*, 1−26.

(14) Hu, Y. P.; Zhong, Y. Q.; Chen, Z. G.; Chen, C. Y.; Shi, Z.; Zulueta, M. M.; Ku, C. C.; Lee, P. Y.; Wang, C. C.; Hung, S. C. Divergent synthesis of 48 heparan sulfate-based disaccharides and probing the specific sugar-fibroblast growth factor-1 interaction. *J. Am. Chem. Soc.* **2012**, *134*, 20722−20727.

(15) Zulueta, M.; Chyan, C. L.; Hung, S. C. Structural analysis of synthetic heparan sulfate oligosaccharides with fibroblast growth factors and heparin-binding hemagglutinin. *Curr. Opin. Struct. Biol.* **2018**, *50*, 126−133.
(16) Subramani, B.; Shantamurthy, C. D.; Maru, P.; Belekar, M. A.; Mardhekar, S.; Shanmugam, D.; Kikkeri, R. Demystifying a hexuronic acid ligand that recognizes Toxoplasma gondii and blocks its invasion into host cells. *Org. Biomol. Chem.* **2019**, *17*, 4535−4542.
(17) de Paz, J. L.; Noti, C.; Seeberger, P. H. Microarrays of synthetic heparin oligosaccharides. *J. Am. Chem. Soc.* **2006**, *128*, 2766−2767.
(18) Das, S. K.; Mallet, J. M.; Esnault, J.; Driguez, P. A.; Duchaussoy, P.; Sizun, P.; Herault, J. P.; Herbert, J. M.; Petitou, M.; Sinaÿ, P. Synthesis of conformationally locked L-iduronic acid derivatives: direct evidence for a critical role of the skew-boat $^2S_0$ conformer in the activation of antithrombin by heparin. *Chem. −A Eur. J.* **2001**, *7*, 4821−4834.
(19) Nieto, L.; Canales, Á.; Fernández, I. S.; Santillana, E.; González-Corrochano, R.; Redondo-Horcajo, M.; Cañada, F. J.; Nieto, P.; Martín-Lomas, M.; Giménez-Gallego, G.; Jiménez-Barbero, J. Heparin modulates the mitogenic activity of fibroblast growth factor by inducing dimerization of its receptor. a 3D view by using NMR. *ChemBioChem* **2013**, *14*, 1732−1744.
(20) Munoz-Garcia, J. C.; Corzana, F.; de Paz, J. L.; Angulo, J.; Nieto, P. M. Conformations of the iduronate ring in short heparin fragments described by time-averaged distance restrained molecular dynamics. *Glycobiology* **2013**, *23*, 1220−1229.
(21) Muñoz-García, J. C.; López-Prados, J.; Angulo, J.; Díaz-Contreras, I.; Reichardt, N.; de Paz, J. L.; Martín-Lomas, M.; Nieto, P. M. Effect of the substituents of the neighboring ring in the conformational equilibrium of iduronate in heparin-like trisaccharides. *Chem. − Eur. J.* **2012**, *18*, 16319−16331.
(22) Hsieh, P. H.; Thieker, D. F.; Guerrini, M.; Woods, R. J.; Liu, J. Uncovering the Relationship between Sulphation Patterns and Conformation of Iduronic Acid in Heparan Sulphate. *Sci. Rep.* **2016**, *6*, 29602.
(23) Casu, B.; Naggi, A.; Torri, G. Heparin-derived heparan sulfate mimics to modulate heparan sulfate-protein interaction in inflammation and cancer. *Matrix. Biol.* **2010**, *29*, 442−452.
(24) Bendersky, V.; Yang, Y.; Brennan, T. V. Immunomodulatory Activities of the Heparan Sulfate Mimetic PG545. *Adv. Exp. Med. Biol.* **2020**, *1221*, 461−470.
(25) Chhabra, M.; Ferro, V. PI-88 and Related Heparan Sulfate Mimetics. *Adv. Exp. Med. Biol.* **2020**, *1221*, 473−491.
(26) Nonaka, M.; Bao, X.; Matsumura, F.; Gotze, S.; Kandasamy, J.; Kononov, A.; Broide, D. H.; Nakayama, J.; Seeberger, P. H.; Fukuda, M. Synthetic di-sulfated iduronic acid attenuates asthmatic response by blocking T-cell recruitment to inflammatory sites. *Proc. Natl. Acad. Sci. U. S. A.* **2014**, *111*, 8173−8178.
(27) Nahain, A. A.; Ignjatovic, V.; Monagle, P.; Tsanaktsidis, J.; Ferro, V. Heparin mimetics with anticoagulant activity. *Med. Res. Rev.* **2018**, *38*, 1582−1613.
(28) Chhabra, M.; Doherty, G. G.; See, N. W.; Gandhi, N. S.; Ferro, V. From Cancer to COVID-19: A Perspective on Targeting Heparan Sulfate-Protein Interactions. *Chem. Rec.* **2021**, *21*, 1−16.
(29) Afosah, D. K.; Al-Horani, R. A. Sulfated Non-Saccharide Glycosaminoglycan Mimetics as Novel Drug Discovery Platform for Various Pathologies. *Curr. Med. Chem.* **2020**, *27*, 3412−3447.
(30) Shanthamurthy, C. D.; Kikkeri, R. Linear Synthesis of *De* novo Oligo-Iduronic Acid. *Eur. J. Org. Chem.* **2019**, *2019*, 2950.
(31) Jain, P.; Shanthamurthy, C. D.; Leviatan Ben-Arye, S.; Woods, R. J.; Kikkeri, R.; Padler-Karavani, V. Discovery of rare sulfated *N*-unsubstituted glucosamine based heparan sulfate analogs selectively activating chemokines. *Chem. Sci.* **2021**, *12*, 3674−3681.
(32) Anand, S.; Mardhekar, S.; Raigawali, R.; Mohanta, N.; Jain, P.; Shanthamurthy, C. D.; Gnanaprakasam, C.; Kikkeri, R. Continuous-Flow Accelerated Sulfation of Heparan Sulfate Intermediates. *Org. Lett.* **2020**, *22*, 3402−3406.
(33) Lu, L. D.; Shie, C. R.; Kulkarni, S. S.; Pan, G. R.; Lu, X. A.; Hung, S. C. Synthesis of 48 disaccharide building blocks for the assembly of a heparin and heparan sulfate oligosaccharide library. *Org. Lett.* **2006**, *8*, 5995−5998.
(34) Haasnoot, C.; de Gelder, R.; Kooijman, H.; Kellenbach, E. R. The conformation of the idopyranose ring revisited: How subtle O-substituent induced changes can be deduced from vicinal ^{1}H-NMR coupling constants. *Carbohydr. Res.* **2020**, *496*, No. 108052.
(35) Hricovíni, M.; Guerrini, M.; Torri, G. NMR of sulfated oligo- and polysaccharides. In *NMR spectroscopy of glycoconjugates*; Wiley-VCH: 2002; pp. 189−229.
(36) Angulo, J.; Hricovíni, M.; Gairi, M.; Guerrini, M.; de Paz, J. L.; Ojeda, R.; Martín-Lomas, M.; Nieto, P. M. Dynamic properties of biologically active synthetic heparin-like hexasaccharides. *Glycobiology* **2005**, *15*, 1008−1015.
(37) Mulloy, B.; Forster, M. J. Conformation and dynamics of heparin and heparan sulfate. *Glycobiology* **2000**, *10*, 1147−1156.
(38) Tebbutt, N.; Pedersen, M. W.; Johns, T. G. Targeting the ERBB family in cancer: couples therapy. *Nat. Rev. Cancer* **2013**, *13*, 663−673.
(39) Sigismund, S.; Avanzato, D.; Lanzetti, L. Emerging functions of the EGFR in cancer. *Mol. Oncol.* **2018**, *12*, 3−20.
(40) Wang, L.; Huang, Y.; Pan, K.; Jiang, X.; Liu, C. Osteogenic responses to different concentrations/ratios of BMP-2 and bFGF in bone formation. *Ann. Biomed. Eng.* **2010**, *38*, 77−87.
(41) Jain, P.; Shanthamurthy, C. D.; Leviatan Ben-Arye, S.; Yehuda, S.; Nandikol, S. S.; Thulasiram, H. V.; Padler-Karavani, V.; Kikkeri, R. Synthetic heparan sulfate ligands for vascular endothelial growth factor to modulate angiogenesis. *Chem. Commun.* **2021**, *57*, 3516−3519.
(42) Guglieri, S.; Hricovíni, M.; Raman, R.; Polito, L.; Torri, G.; Casu, B.; Sasisekharan, R.; Guerrini, M. Minimum FGF2 binding structural requirements of heparin and heparan sulfate oligosaccharides as determined by NMR spectroscopy. *Biochemistry* **2008**, *47*, 13862−13869.
(43) de Paz, J. L.; Noti, C.; Böhm, F.; Werner, S.; Seeberger, P. H. Potentiation of fibroblast growth factor activity by synthetic heparin oligosaccharide glycodendrimers. *Chem. Biol.* **2007**, *14*, 879−887.
(44) Rodrigo, A. C.; Barnard, A.; Cooper, J.; Smith, D. K. Self-assembling ligands for multivalent nanoscale heparin binding. *Angew. Chem. Int. Ed.* **2011**, *50*, 4675−4679.
(45) Tyler, P. C.; Guimond, S. E.; Turnbull, J. E.; Zubkova, O. V. Single-entity heparan sulfate glycomimetic clusters for therapeutic applications. *Angew. Chem. Int. Ed.* **2015**, *54*, 2718−2723.
(46) Koide, H.; Yoshimatsu, K.; Hoshino, Y.; Lee, S. H.; Okajima, A.; Ariizumi, S.; Narita, Y.; Yonamine, Y.; Weisman, A. C.; Nishimura, Y.; Oku, N.; Miura, Y.; Shea, K. J. A polymer nanoparticle with engineered affinity for a vascular endothelial growth factor ($VEGF_{165}$). *Nat. Chem.* **2017**, *9*, 715−722.
(47) Jain, P.; Shanthamurthy, C. D.; Chaudhary, P. M.; Kikkeri, R. Rational designing of glyco-nanovehicles to target cellular heterogeneity. *Chem. Sci.* **2021**, *12*, 4021−4027.
(48) Graells, J.; Vinyals, A.; Figueras, A.; Llorens, A.; Moreno, A.; Marcoval, J.; Jesus Gonzalez, F.; Fabra, A. Overproduction of VEGF concomitantly expressed with its receptors promotes growth and survival of melanoma cells through MAPK and PI3K signaling. *J. Invest. Dermatol.* **2004**, *123*, 1151−1161.
(49) Sangabathuni, S.; Murthy, R. V.; Gade, M.; Bavireddi, H.; Toraskar, S.; Sonar, M. V.; Ganesh, K. N.; Kikkeri, R. Modeling Glyco-Collagen Conjugates Using a Host-Guest Strategy to Alter Phenotypic Cell Migration and in Vivo Wound Healing. *ACS Nano* **2017**, *11*, 11969−11977.
(50) Zhao, W.; McCallum, S. A.; Xiao, Z.; Zhang, F.; Linhardt, R. J. Binding affinities of vascular endothelial growth factor (VEGF) for heparin-derived oligosaccharides. *Biosci. Rep.* **2012**, *32*, 71−81.

https://doi.org/10.1021/acschembio.1c00582
ACS Chem. Biol. 2021, 16, 2481−2489